# Thickness ratio and $d_{33}$ effects on flexible piezoelectric unimorph energy conversion

2016 Smart Mater. Struct. 25 035037

(http://iopscience.iop.org/0964-1726/25/3/035037)

**IOP** Publishing Smart Materials and Structures

Smart Mater. Struct. **25** (2016) 035037 (19pp) doi:10.1088/0964-1726/25/3/035037

# Thickness ratio and $d_{33}$ effects on flexible piezoelectric unimorph energy conversion

**Taewoo Ha**[1,2], **John X J Zhang**[3] and **Nanshu Lu**[1]

[1] Center for Mechanics of Solids, Structures, and Materials, Department of Aerospace Engineering and Engineering Mechanics, Department of Biomedical Engineering, Texas Materials Institute, The University of Texas, Austin, TX 78712, USA
[2] Department of Electrical and Computer Engineering, The University of Texas, Austin, TX 78712, USA
[3] Thayer School of Engineering, Dartmouth College, Hanover, NH 03755, USA

E-mail: nanshulu@utexas.edu

Received 13 October 2015, revised 11 January 2016
Accepted for publication 18 January 2016
Published 22 February 2016

## Abstract

Piezoelectric unimorphs are bilayer structures where a blanket piezoelectric film (with top and bottom electrodes) is uniformly laminated on an inactive but flexible substrate. Because of their simple construction and flexibility, unimorphs are widely used as a key element in flexible sensors and actuators. The response of a unimorph is governed by the material properties of the film and the substrate as well as their geometric parameters. For low frequency biological energy harvesting, structural optimization is critical due to the dimensional confinement imposed by curvilinear and deformable bio-tissues. Here we report a comprehensive theoretical framework to investigate the effects of the film-to-substrate thickness ratio on voltage, charge, and energy outputs when the unimorph is subjected to eight different boundary/loading conditions. A broad class of power generators can be designed using such a framework under the assumption that the unimorph length is very large compared to its thickness, where the only dimensionless variable is the film-to-substrate thickness ratio. We show that the analytical and finite element modeling results are in excellent agreement. For not so thin unimorphs, there is non-zero normal stress in the thickness direction ($\sigma_3$) and $d_{33}$ can play a significant role in this case. Non-monotonic dependence of voltage and energy generation on thickness ratio has been found in some cases and optimum thickness ratio for unimorph generator can be predicted. When the unimorph is actuated by voltage applied across the piezo-film thickness, non-monotonic maximum deflection versus thickness ratio is also found. This work provides new physical insights on unimorphs and analytical solutions that can be used for the structural design and optimization of unimorphs under different boundary/loading conditions.

Keywords: piezoelectric, unimorph, flexible, thickness ratio, $d_{33}$, energy, generator

(Some figures may appear in colour only in the online journal)

## 1. Introduction

Piezoelectric materials convert electrical pulses from or to mechanical vibrations [1]. Such electromechanical energy conversion is ubiquitous in both inorganic materials and biological systems. Piezoelectric materials in nature can be ceramic or polymeric: ceramic piezoelectric materials including lead zirconate titanate (PZT) [2], zinc oxide (ZnO) [3], barium titanate (BTO) [4] are known to have large intrinsic piezoelectric coefficients but they are mechanically stiff and brittle. Polymeric piezoelectric materials such as polyvinylidene fluoride (PVDF) [5] and porous electromechanical film (EMFi) [6] are intrinsically more compliant, but their piezoelectric coefficients are one order smaller than those of the ceramic ones [7]. Both kinds of piezoelectric materials have found wide applications in sensing, actuation, and energy harvesting [8] because of their unique combination of mechanical form factors and energy transduction capabilities.

Mechanical energy from nature, machines, and the human body provides an excellent alternative as clean, non-depletable power sources. Many ambient sources of mechanical energy, including wind [9], water flow [10], and human motion [11], have been collected by piezoelectric devices. With the emergence of wearable electronics and bio-integrated electronics [12], flexible and stretchable generators that can harvest power from the natural processes of the body such as the vibration of muscles, lungs, and heart have attracted growing interest [13]. Examples include ZnO nanowire based nanogenerators [14], buckled PZT nanoribbon based stretchable biocompatible energy harvester [15], and BTO [16] and ZnO [17] thin film based bendable nanogenerators, as well as PVDF based nanogenerators and biosensors [18–21]. Although the power generated is usually on the order of microwatts to milliwatts, which may not be sufficient to power most wearable or implantable devices, the generators can at least be used to recharge batteries.

Theoretical models for piezoelectric energy harvesters are widely available in the literature [22–25]. Two major threads of energy harvesting optimization theories are resonance frequency analysis and structural analysis. As mechanical activities of the human body exhibit low frequency (1–30 Hz) [26], resonance frequency optimization is less relevant here. Instead, structural optimization becomes an important problem due to the dimensional confinement imposed by the curvilinear and deformable human body and organs [27]. Constituent equations for a cantilever unimorph under static conditions have been established by Smits and Choi [23]. Using those equations, the effects of thickness ratio and elastic mismatch of a cantilever unimorph have been theoretically investigated by Wang *et al* [22], who found a non-monotonic relationship between thickness ratio and electric outputs. Subsequently, several numerical studies on the effect of thickness ratio of unimorphs have been reported [28–30].

Existing unimorph models [22, 23, 31] are mostly limited to cantilever configurations and the $d_{33}$ contribution has been neglected because $\sigma_3$ is always assumed to be zero. However, unimorphs can also operate under the boundary conditions of pure bending or simple–simple support and can be subjected to a variety of types of load or displacement excitations. Moreover, $\sigma_3$ is non-zero for thick unimorphs and may make significant contributions to the outputs. To find a remedy for the aforementioned deficiencies, we derive closed-form solutions for unimorphs in eight different boundary/loading conditions. To validate our theory, finite element modeling (FEM) was performed using COMSOL Multiphysics. Non-monotonic electrical outputs versus thickness ratio curves are found for several boundary value problems. To resolve the discrepancy between theoretical and FEM results for some scenarios, the $d_{33}$ effect had to be taken into consideration. Simple models to determine average $\sigma_3$ along beam length has been proposed and turn out to be very effective in accounting for the $d_{33}$ contribution. The $d_{33}$ effect is found to be more significant as piezo-layer thickness increases. When simple–simple and cantilever unimorphs are subjected to voltage excitation, non-monotonic deflection versus thickness ratio curves are obtained and the $d_{33}$ effect is also revealed. Overall, this work provides new physical insights on flexible unimorphs and analytical solutions that can be used for the structural optimization of unimorphs under different boundary/loading conditions.

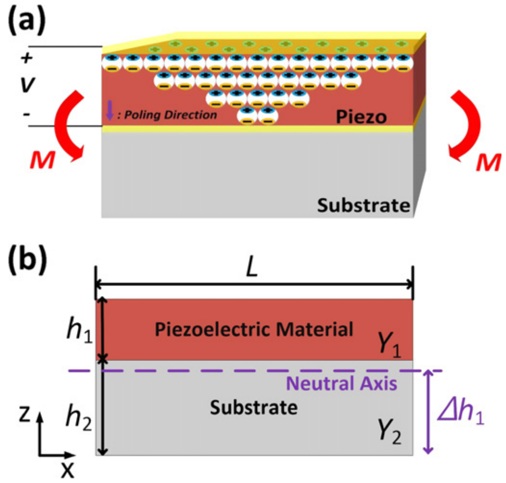

**Figure 1.** (a) A schematic of a unimorph generator. When subjected to bending moment, the polarization density varies linearly along the thickness direction. (b) Illustration of basic variables: the thickness of the piezo-layer and the polymer substrate is $h_1$ and $h_2$, respectively, the Young's modulus is $Y_1$ and $Y_2$, respectively, and the length of the unimorph is labeled as $L$. The neutral axis of the bilayer is located $\Delta h_1$ away from the bottom of the substrate, where $\Delta$ is a dimensionless parameter given in equation (1).

Our paper is organized as follows. Section 2 describes material properties and boundary/loading conditions. Section 3 offers both analytical and FEM results of unimorph generators under eight different boundary/loading conditions. Section 4 discusses the effect of elastic mismatch and unimorph actuators. Concluding remarks are drawn in section 5.

## 2. Problem description

Figure 1(a) is the schematic of a piezoelectric unimorph generator with the piezoelectric layer poled downward. When a bending moment is applied to this unimorph as illustrated in figure 1(a), a dielectric polarization in the same direction as the poling direction will be induced by the bending deformation of the piezoelectric layer. Suppose the piezoelectric layer and the substrate have thicknesses of $h_1$ and $h_2$ and Young's moduli of $Y_1$ and $Y_2$, as labeled in figure 1(b), calculating the voltage, charge, and power output of such a unimorph first requires the determination of the neutral axis and the effective second moment of inertia of the bilayer. The distance from the neutral axis to the bottom surface of the substrate is represented by $\Delta h_1$, as labeled in figure 1(b), where $\Delta$ has been given by [32]

$$\Delta = \frac{1+2\Sigma\eta + \Sigma\eta^2}{2\eta(1+\Sigma\eta)}, \tag{1}$$

where $\Sigma = \overline{Y_1}/\overline{Y_2}$ is the film-to-substrate modulus ratio with $\bar{Y} = Y/(1 - \nu^2)$ being the plane strain modulus, $Y$ being the Young's modulus, $\nu$ being the Poisson's ratio, and $\eta = h_1/h_2$ is the film-to-substrate thickness ratio.

The effective second moment of inertia of the bilayer is given by [32]

$$I = {h_2}^3\left\{\Sigma\left[\eta(\Delta\eta - 1)^2 - \eta^2(\Delta\eta - 1) + \frac{\eta^3}{3}\right] + \Delta\eta(\Delta\eta - 1) + \frac{1}{3}\right\} = {h_2}^3\bar{I}, \tag{2}$$

where $\bar{I}$ represents the non-dimensional second moment of inertia and hence the bending stiffness of the unimorph can be written as $\bar{Y}_2 I$. For given piezoelectric and substrate materials (i.e., $\Sigma$ fixed), the only dimensionless variable in the problem is the thickness ratio $\eta$, whose effect is the focus of this study.

For eight different boundary/loading conditions, solutions have been obtained through both 2D plane strain linear piezoelectric theory and FEM. Before describing the theory in section 3, the material parameters and model setup in the commercial FEM software, COMSOL Multiphysics 4.4, are summarized here. We choose Kapton as a representative inactive flexible substrate material with Young's modulus of 2.5 GPa, Poisson's ratio of 0.34, and mass density of 1420 kg m$^{-3}$, assuming it is isotropic [33]. For the piezoelectric layer, we choose poly(vinylidene fluoride-co-trifluoro ethylene) (PVDF-TrFE) because of its popularity and mechanical robustness. Furthermore, PVDF-TrFE (75/25) has well-established experimental data of mass density (1879 kg m$^{-3}$ [34]), elastic compliance, relative permittivity, and piezoelectric coefficients [35]:

-Elastic compliance tensor

$$s^{\mathrm{E}} = \begin{bmatrix} 3.32 & -1.44 & -0.89 & 0 & 0 & 0 \\ -1.44 & 3.24 & -0.86 & 0 & 0 & 0 \\ -0.89 & -0.86 & 3.00 & 0 & 0 & 0 \\ 0 & 0 & 0 & 94.0 & 0 & 0 \\ 0 & 0 & 0 & 0 & 96.3 & 0 \\ 0 & 0 & 0 & 0 & 0 & 14.4 \end{bmatrix} \times 10^{-10}\,\mathrm{Pa}^{-1}, \tag{3}$$

where $Y_1 = 1/s_{11}$ and $v_1 = -s_{13}/s_{11}$ are found to be 3 GPa and 0.268 GPa, respectively.

-Permittivity matrix

$$\varepsilon^{\mathrm{T}} = \begin{bmatrix} 7.4 & 0 & 0 \\ 0 & 7.95 & 0 \\ 0 & 0 & 7.9 \end{bmatrix} \times \varepsilon_0, \tag{4}$$

where $\varepsilon_0 = 8.85 \times 10^{-12}\,\mathrm{F\,m^{-1}}$ is the vacuum permittivity. Hence the relative permittivity in the thickness direction is $\varepsilon_{\mathrm{p}} = 7.9$.

-Piezoelectric coupling tensor

$$d = \begin{bmatrix} 0 & 0 & 0 & 0 & -36.3 & 0 \\ 0 & 0 & 0 & -40.6 & 0 & 0 \\ 10.7 & 10.1 & -33.5 & 0 & 0 & 0 \end{bmatrix} \times 10^{-12}\ \mathrm{C \cdot N^{-1}}. \tag{5}$$

When the film is fixed to be PVDF-TrFE and the substrate to be Kapton, then the elastic mismatch $\Sigma = \overline{Y_1}/\overline{Y_2}$ is fixed to be 1.148. To study the effect of the film-to-substrate thickness ratio, the Kapton thickness is fixed to be 25 $\mu$m whereas the thickness of PVDF-TrFE varies from 0.5 to 20 $\mu$m with an incremental step of 0.5 $\mu$m. While the mechanical boundary conditions vary from case to case, the electrostatic boundary conditions remain the same for all eight cases of generators in section 3. The top surface of the piezo-layer is set as the ground and voltage is collected and averaged at the bottom of the piezo-layer. The absolute value of charge on top and bottom surfaces are collected and averaged to yield the total charge. All other boundaries are set to zero charge. When meshing the model in COMSOL, we selected 'mapped mesh' method with the maximum element size of 0.5 $\mu$m and the minimum element size of 0.01 $\mu$m.

## 3. Formulation and results of generators

In this section, the analytical formulation of piezoelectric unimorph generator under eight different boundary/loading conditions will be provided and the voltage, charge density, and energy density outputs will be predicted as functions of the film-to-substrate thickness ratio. When necessary, $d_{33}$ effects will be considered and the substrate thickness-to-length ratio is an added variable. Analytical results and FEM results will be compared and discussed.

### *3.1. Pure bending under constant moment (PB-M)*

Figure 2(a) illustrates the boundary and loading conditions of a unimorph subjected to pure bending under constant bending moment $M_0$ (PB-M). Based on Euler–Bernoulli beam theory, the only non-zero stress component in this unimorph will be bending induced normal stress in $x$ direction and its vertical distribution is given by

$$\sigma_1 = \frac{M_0(z - \Delta h_1)}{{h_2}^3}\frac{\Sigma}{\bar{I}}, \tag{6}$$

where $\Delta$ is given in equation (1) and $\bar{I}$ in equation (2). The subscript 1 in $\sigma$ denotes $x$ direction and 3 will be used to denote $z$ direction, where $x$ and $z$ directions are defined in figure 1(b).

Based on the linear piezoelectric theory [36], deformation induced polarization density is proportional to stress through the piezoelectric coefficient, i.e. $P_i = d_{ij}\sigma_j$ ($i = 1,\ 2,\ 3,\ j = 1,\ 2,\dots,6$), therefore $z$ direction polarization density is given by

$$P_3 = \frac{d_{31}M_0(z - \Delta h_1)}{{h_2}^3}\frac{\Sigma}{\bar{I}}. \tag{7}$$

Since charges are only collected from the top and bottom surface electrodes of the piezo-layer, only top ($z = h_1 + h_2$) and bottom ($z = h_2$) surface polarization density will be considered to calculate the total amount of charges.

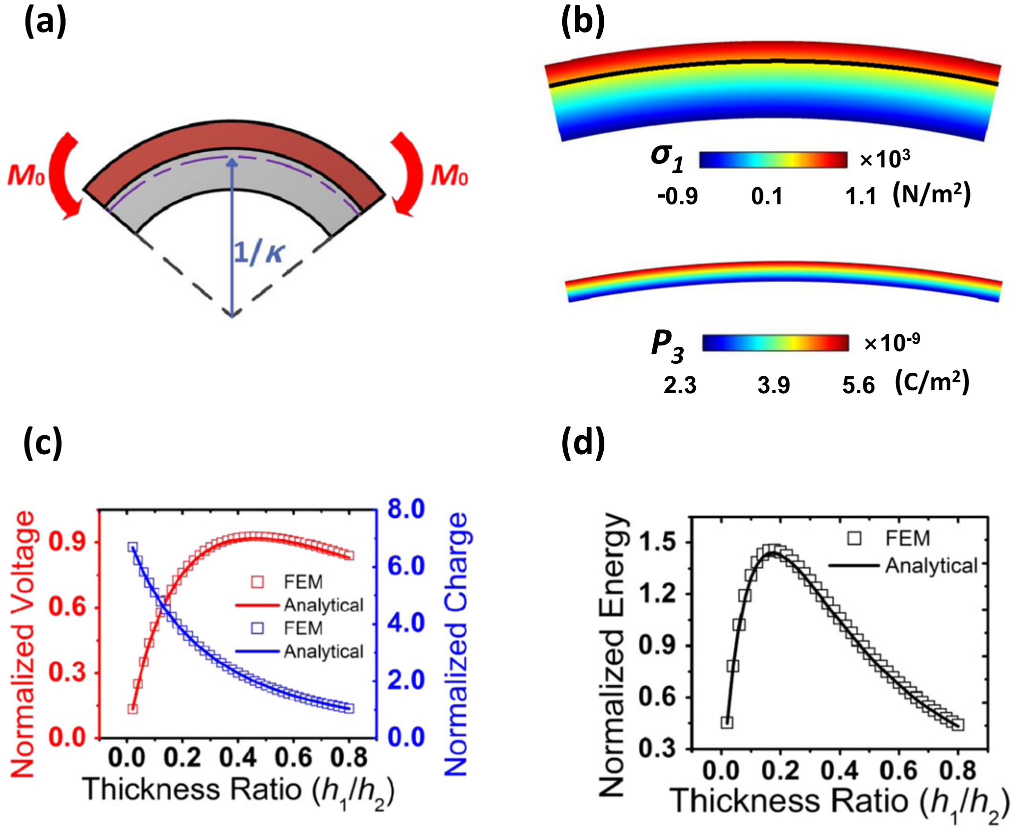

**Figure 2.** (a) A schematic for the pure bending with constant bending moment (PB-M) case which is discussed in section 3.1. (b) FEM results of $\sigma_1$ and $P_3$ when $M_0 = 1 \times 10^{-7}$ N m. (c) The analytical (curves) and FEM (markers) results of normalized voltage and charge density as functions of the thickness ratio ($\eta = h_1/h_2$). (d) The analytical and FEM results of normalized energy density as a function of the thickness ratio.

As the total amount of charges and polarization density are related through $Q = -\int \bar{a}_n \cdot \bar{P} \mathrm{d}S$, where $\bar{a}_n$ stands for the surface normal vector and $S$ stands for the overall surface area ($S = L$ in our plane strain model), the effective charge output, which is defined as $Q_{\mathrm{PB}-M} = (|Q_{\mathrm{Top}}| + |Q_{\mathrm{Bot}}|)/2$ can be expressed as

$$Q_{\mathrm{PB}-M} = \frac{d_{31}LM_0}{h_2{}^2}\left[\frac{\Sigma}{\bar{I}}\left(1 + \frac{\eta}{2} - \Delta\eta\right)\right]. \tag{8}$$

Therefore surface charge density can be readily given by $\rho = Q/S$, i.e.

$$\rho_{\mathrm{PB}-M} = \frac{d_{31}M_0}{h_2{}^2}\left[\frac{\Sigma}{\bar{I}}\left(1 + \frac{\eta}{2} - \Delta\eta\right)\right]. \tag{9}$$

Through the definition of capacitance $C = Q/V$, voltage is given by $V = Q/C$ where $C = \varepsilon_{\mathrm{p}}{}'L/h_1$, with $\varepsilon_{\mathrm{p}}{}'$ being the effective permittivity of the piezoelectric material [23]:

$$\varepsilon_{\mathrm{p}}{}' = \varepsilon_{\mathrm{p}}\left\{1 \pm \frac{d_{31}{}^2}{6\bar{Y}_1\varepsilon_{\mathrm{p}}}\left(\frac{\Sigma\eta^3 + 1}{\eta + 1}\right)\left(1 + \frac{\eta}{2} - \Delta\eta\right)\frac{1}{\bar{I}}\right\}, \tag{10}$$

where the sign depends on the poling direction. Hence the output voltage is given by

$$V_{\mathrm{PB}-M} = \frac{d_{31}M_0}{\varepsilon_{\mathrm{p}}{}'h_2}\left[\frac{\Sigma\eta}{\bar{I}}\left(1 + \frac{\eta}{2} - \Delta\eta\right)\right]. \tag{11}$$

Finally the generated energy density can be calculated by $U = \rho V/2$, i.e.

$$U_{\mathrm{PB\_}M} = \frac{1}{2}\frac{d_{31}{}^2M_0{}^2}{\varepsilon_{\mathrm{p}}{}'h_2{}^3}\left[\eta\left(\frac{\Sigma}{\bar{I}}\right)^2\left(1 + \frac{\eta}{2} - \Delta\eta\right)^2\right]. \tag{12}$$

It is obvious from equations (9)–(12) that when film and substrate materials are fixed, i.e. when $\Sigma$ is fixed, dimensionless $\rho$, $V$, and $U$ will just depend on the thickness ratio, $\eta$, which will be plotted together with FEM results.

Our FEM model implements the pure bending condition as illustrated by figure 2(a) with the substrate being Kapton, piezoelectric layer being PVDF-TrFE and with fixed $h_2 = 25\,\mu$m and $M_0 = 1 \times 10^{-7}$ N m, which is estimated from the change of heart curvature during heart beat [37, 38] times the bending stiffness of the unimorph. Bending moment was applied on each side wall of the beam through the boundary condition named 'rigid connector'. The FEM contour plots of stress and polarization density are given in figure 2(b) with $h_1 = 10\,\mu$m. Both stress and polarization density vary linearly with $z$, as predicted by equations (7) and (8). Charge and voltage can also be directly output from FEM and $U = \rho V/2$ is used to calculate the FEM output of electrical energy density.

Analytical and FEM results are compared in figures 2(c) and (d). Excellent overlap between equations (9) and (11) and FEM results demonstrates a strong validation of our linear piezoelectric theory for unimorphs even without accounting for the $d_{33}$ effect in the formulation ($d_{33}$ is included in FEM). The biggest mismatch between FEM results and equation (11) in figure 2(c) is less than 1.8%, which occurs at the largest $\eta$. The mismatch is due to the breakdown of Bernoulli's beam theory: when $L$ and $h_2$ are fixed and $h_1$ is increased to increase $\eta$, the overall unimorph thickness-to-length ratio increases and $\sigma_3$ can no longer be assumed zero. This effect is more pronounced in cantilever and simply supported unimorphs and will be specifically discussed in section 3.3. It is interesting to see that while the charge density monotonically decays as the piezo-film gets thicker, the voltage output is non-monotonic, with the peak value reached at $\eta = 0.46$. This is due to the tradeoff that under constant moment, increasing $h_1$ will enlarge both distance from neutral axis, which enhances the voltage output, and second moment of inertia, which diminishes the voltage output. Normalized energy density is plotted in figure 2(d). The optimized thickness ratio for maximum energy output is $\eta = 0.18$, which is different from the optimal $\eta$ with maximum voltage output. Therefore, choosing the optimum thickness ratio depends on whether maximum voltage output or energy density is desired.

### 3.2. Pure bending under constant curvature (PB-$\kappa$)

Figure 3 shows the FEM and analytical solutions for the unimorph subjected to pure bending with constant curvature $\kappa_0$ (PB-$\kappa$). Following the same procedures outlined in 3.1 and directly substituting $M_0 = \kappa_0 \overline{Y_2} h_2^3 \bar{I}$ into equations (9) and (11), analytical expressions for the charge density and the voltage output under PB-$\kappa$ are

$$\rho_{\mathrm{PB}-\kappa} = d_{31}\overline{Y_1}\kappa_0 h_2\left(1 + \frac{\eta}{2} - \Delta\eta\right) \tag{13}$$

and

$$V_{\mathrm{PB}-\kappa} = \frac{d_{31}\overline{Y_1}\kappa_0 {h_2}^2}{{\varepsilon_{\mathrm{p}}}'}\left[\eta\left(1 + \frac{\eta}{2} - \Delta\eta\right)\right], \tag{14}$$

respectively. Figure 3(b) shows the FEM results of $\sigma_1$ and $P_3$ where the piezo-layer is 10 $\mu$m thick and $\kappa_0$ is fixed as 2 $\mathrm{m}^{-1}$.

Figure 3(c) shows the normalized voltage and charge density under the PB-$\kappa$ condition. While the charge density monotonically decays with increasing $\eta$, which is similar to the PB-M result, the voltage output increases with increasing $\eta$, which is very different from the PB-M result. This is because under constant curvature, the second moment of inertia no longer shows up in the denominator of the voltage equation. Figure 3(d) plots the normalized electrical energy density ($U = \rho V/2$) generated under the PB-$\kappa$ condition, which monotonically increases with $\eta$.

### 3.3. Effects of $d_{33}$ in cantilever and simply supported unimorphs

While working on cantilever and simply supported unimorphs, we realized that unlike unimorphs subjected to pure bending, there is non-zero $\sigma_3$ in cantilever and simply supported unimorphs. Since $\sigma_3$ generates additional $P_3$ through $d_{33}$, it is important to account for its contribution when analyzing cantilever and simply supported unimorphs. Figure 4(a) left panel depicts a cantilever unimorph subjected to uniformly distributed load (the C–Q condition). A free body diagram is drawn on the right panel when we make a cut along Line AB. It is clear that the applied distributed load has to be balanced by the reaction shear force applied by the wall and the normal force on the $AB$ plane. Let $\sigma_3$ be the average normal stress on the $AB$ plane, the force balance equation is hence established in the bottom of the free body diagram. Since the shear stress is parabolically distributed along the left surface as

$$\tau(z) = q_{\mathrm{c}}L/(2h_2\bar{I}) \cdot [(1 + \eta - \Delta\eta)^2 - (z/h_2 - \Delta\eta)^2], \tag{15}$$

$\sigma_3$ is a function of $z$.

Figure 4(b) illustrates the case where a cantilever unimorph is subjected to point load at the end (the C–F condition). Similar to the C–Q condition, the applied point load is fully balanced by the reaction shear force applied by the wall and the normal force on the $AB$ plane. Again the average normal stress $\sigma_3$ on the $AB$ plane can be calculated by the force balance equation in the bottom of the free body diagram where $\tau(z)$ is simply given by equation (15) with $q_{\mathrm{c}}L$ replaced by $F_{\mathrm{c}}$.

Similarly, for simply supported unimorphs subjected to uniformly distributed load (SS–Q condition) and point load at the center (SS–F condition), figures 4(c) and (d) offer the free body diagrams that help determine the average $\sigma_3$ along the AB plane, both of which are constants, which is different from the cantilever unimorphs.

### 3.4. Cantilever unimorph under uniformly distributed load (C–Q)

The expression for the moment distribution in C–Q condition is

$$M(x) = \frac{q_{\mathrm{c}}(L^2 - 2Lx + x^2)}{2}, \tag{16}$$

where the $q_{\mathrm{c}}$ is the distributed load per unit length, as labeled in figure 5(a). The charge density and voltage output can be derived following the same procedure outlined in section 3.1:

$$\rho_{\mathrm{C-Q}} = \frac{d_{31}\, q_{\mathrm{c}}L^2}{6{h_2}^2}\left[\frac{\Sigma}{\bar{I}}\left(1 + \frac{\eta}{2} - \Delta\eta\right)\right] \tag{17}$$

and

$$V_{\mathrm{C-Q}} = \frac{d_{31}\, q_{\mathrm{c}}L^2}{6{\varepsilon_{\mathrm{p}}}'h_2}\left[\frac{\Sigma\eta}{\bar{I}}\left(1 + \frac{\eta}{2} - \Delta\eta\right)\right], \tag{18}$$

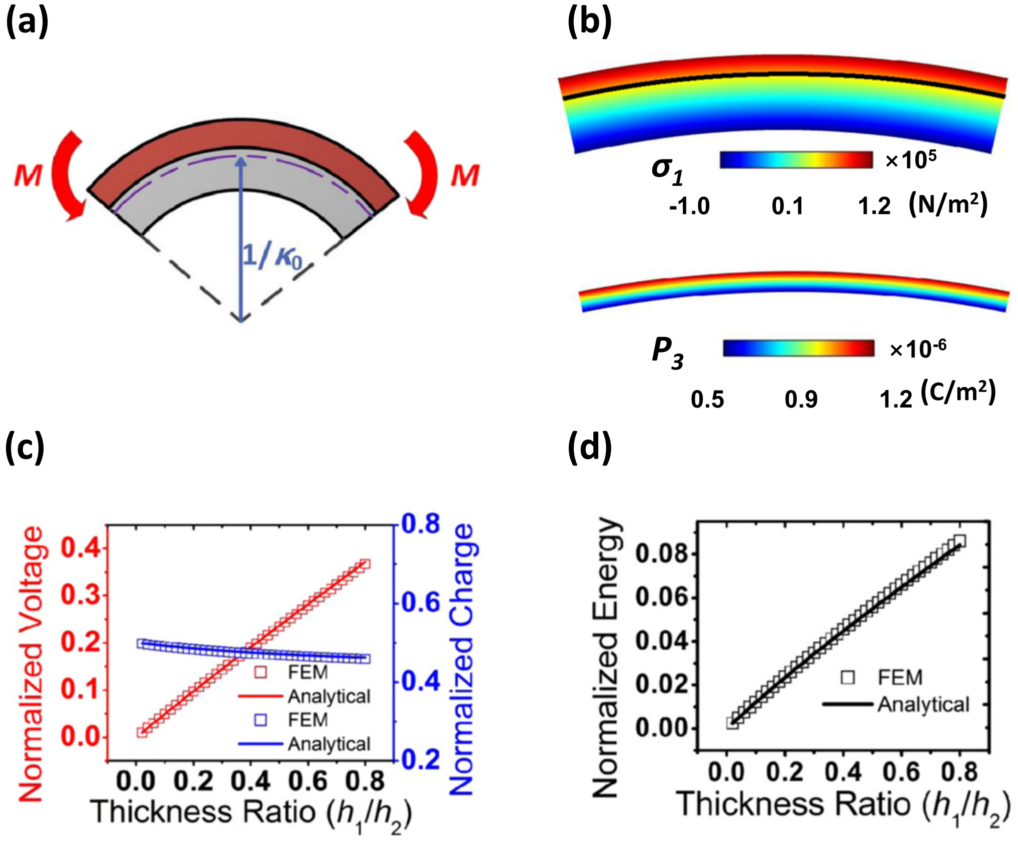

**Figure 3.** (a) A schematic for the pure bending with constant bending curvature (PB-$\kappa$) case which is discussed in section 3.2. (b) FEM results of $\sigma_1$ and $P_3$ when $\kappa_0 = 2\ \text{m}^{-1}$. (c), (d) The analytical and FEM results of normalized voltage, charge density, and energy density as functions of the thickness ratio.

respectively, where the contribution of $\sigma_3$ is not yet considered. Comparing equation (17) with (9) and (18) with (11), simply substituting $M_0 = q_c L^2/6$ can readily convert the PB-M solution to the C–Q solution. But in the C–Q solution, $L$ is a new variable that does not exist in the PB-M solution.

Figure 5(b) shows the FEM contour plots of $\sigma_1$ and $P_3$ when the piezo-layer thickness is 10 $\mu$m under the C–Q condition and $d_{33}$ is included. The uniformly distributed load is chosen such that the average moment in the C–Q condition $M = q_c L^2/6$ equals to the moment applied in the PB-M condition. When we plot equations (17) and (18) as dash–dot line against FEM results as shown in figure 5(c), a clear mismatch can be observed, especially when $h_1/h_2$ is large. This is because the polarization density due to non-zero $\sigma_3$ was not accounted for. According to the equilibrium equation given in figure 4(a), average $\sigma_3$ in the C–Q condition can be expressed as

$$\sigma_3 = -q_c\left\{1 - \frac{1}{\bar{I}}\left[\frac{1}{3}(1+\eta-\Delta\eta)^3 - \frac{1}{2}(1+\eta-\Delta\eta)^2\left(\frac{z}{h_2}-\Delta\eta\right) + \frac{1}{6}\left(\frac{z}{h_2}-\Delta\eta\right)^3\right]\right\}. \tag{19}$$

Subsequently, the polarization density induced by $\sigma_3$ through the $d_{33}$ coefficient is

$$P_{3\_d_{33}} = -d_{33}q_c\left\{1 - \frac{1}{\bar{I}}\left[\frac{1}{3}(1+\eta-\Delta\eta)^3 - \frac{1}{2}(1+\eta-\Delta\eta)^2\left(\frac{z}{h_2}-\Delta\eta\right) + \frac{1}{6}\left(\frac{z}{h_2}-\Delta\eta\right)^3\right]\right\}. \tag{20}$$

Note $d_{33}$ for PVDF-TrFE is a negative value as given in equation (5).

Finally the total charge density and voltage output induced by both $\sigma_1$ and $\sigma_3$ in the C–Q case are

$$\rho'_{\text{C-Q}} = \frac{d_{31}q_c L^2}{6{h_2}^2}\left\{\frac{\Sigma}{\bar{I}}\left[\left(1+\frac{\eta}{2}-\Delta\eta\right) - \frac{d_{33}}{d_{31}}\left(\frac{h_2}{L}\right)^2 \times\left(\frac{12\bar{I} - \eta^2(3+2\eta-3\Delta\eta)}{2\Sigma}\right)\right]\right\} \tag{21}$$

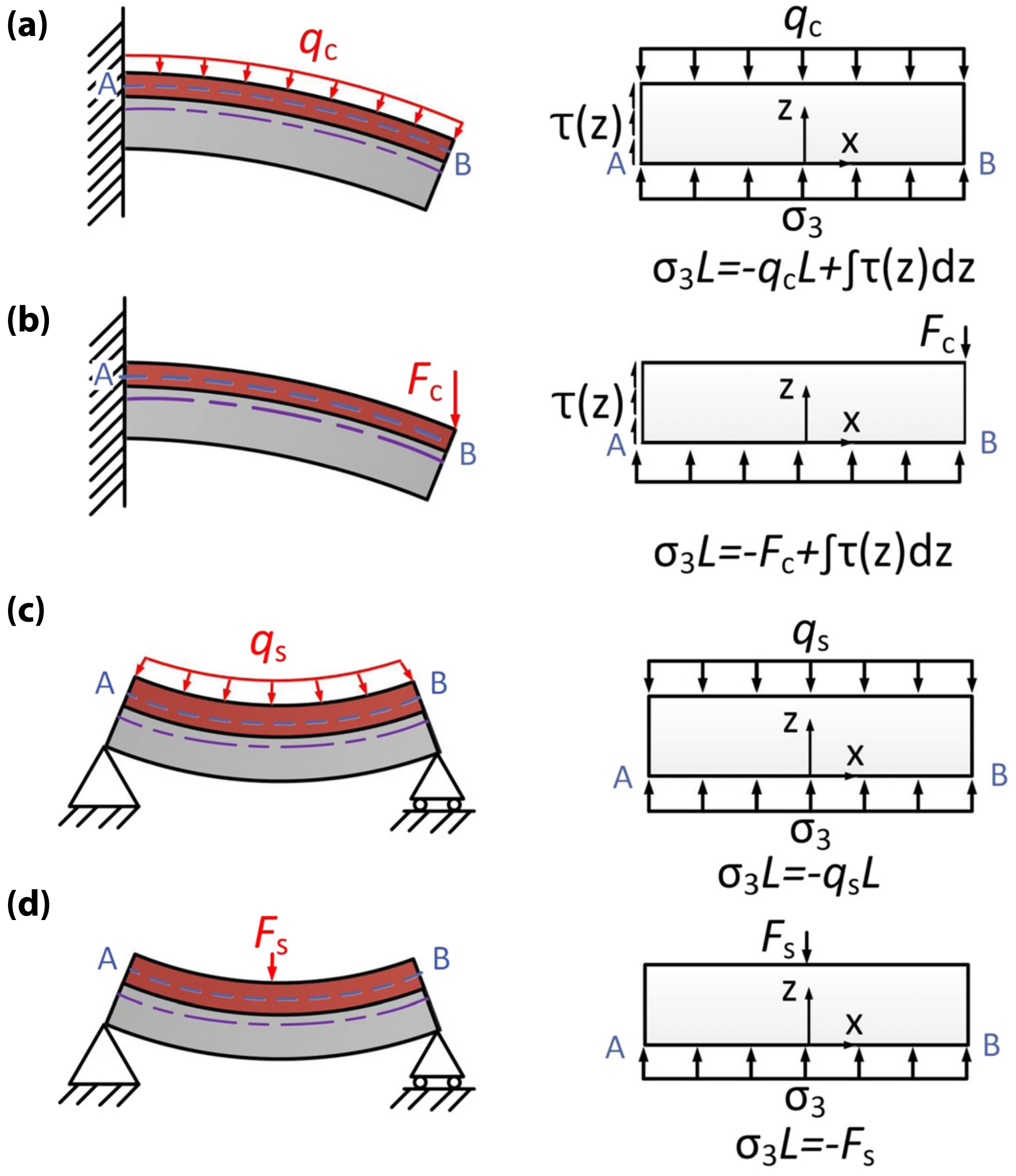

**Figure 4.** Schematics and free body diagrams for calculating average $\sigma_3$ in cantilever and simply supported unimorphs. (a) Cantilever unimorph subjected to uniformly distributed load (C–Q case) where shear stress applied by the left wall has a parabolic distribution. (b) Cantilever unimorph subjected to point load (C–F case) where shear stress applied by the left wall also has a parabolic distribution. (c) Simply supported unimorph subjected to uniformly distributed load (SS–Q case) where $\sigma_3 = -q_s$. (d) Simply supported unimorph subjected to point load (SS–F case) where $\sigma_3 = -F_s/L$.

and

$$V'_{\mathrm{C-Q}} = \frac{d_{31} q_c L^2}{6\varepsilon_p{}' h_2}\left\{\frac{\Sigma\eta}{\bar{I}}\left[\left(1+\frac{\eta}{2}-\Delta\eta\right)-\frac{d_{33}}{d_{31}}\left(\frac{h_2}{L}\right)^2 \times\left(\frac{12\bar{I}-\eta^2(3+2\eta-3\Delta\eta)}{2\Sigma}\right)\right]\right\}, \tag{22}$$

respectively. Note that in both equations the $d_{33}$ term diminishes as the length of the unimorph increases. Plotting equations (21) and (22) as solid curves in figure 5(c) and $U = \rho' V'/2$ as a solid curve in figure 5(d), they have found excellent agreement with the FEM results, until again when $h_1$ is too large for the beam theory to stay valid as discussed before. The optimal $\eta$ for the voltage and the energy density are 0.58 and 0.2, respectively. The optimal $\eta$ for the voltage is slightly shifted compared to PB-M case because of the additional contribution from $\sigma_3$.

Figures 5(e) and (f) show the normalized electric outputs when the boundary and loading conditions stay the same but the piezo-film and the substrate switch position. In this case piezo-layer is still Layer 1 and substrate is still Layer 2, and $\Sigma$, $\eta$ and $\Delta$ given by equation (1) stay the same. In this case the piezo-layer is located below the neutral axis so the sign of $\sigma_1$ is changed. The $\sigma_3$ equation in figure 4(a) is still valid but as the shear force term is larger than the piezo-layer-on-substrate case, the $\sigma_3$ is smaller in the substrate-on-piezo-layer case. As a result, the $\sigma_3$ contribution will be a smaller effect and it will counteract the $\sigma_1$ contribution, as evidenced in

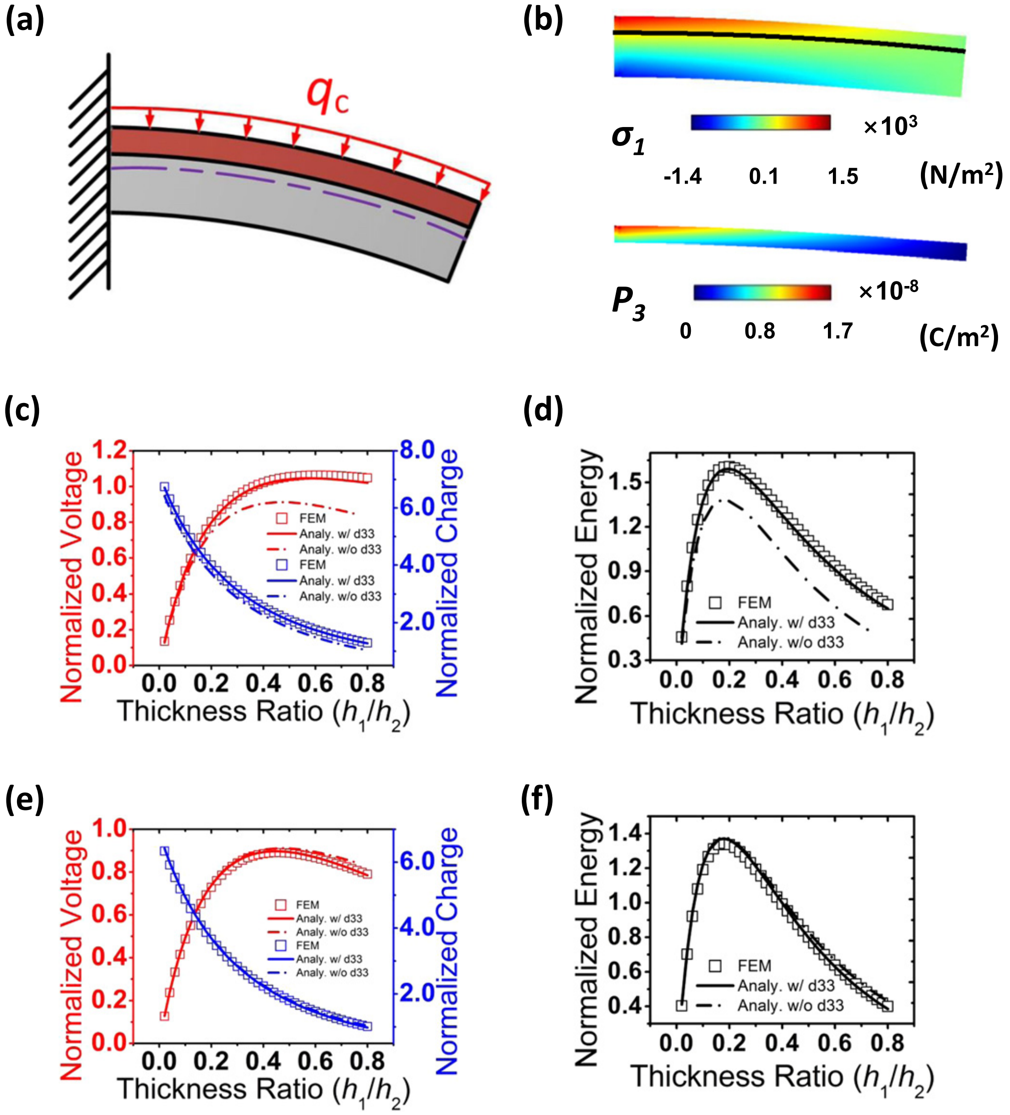

**Figure 5.** (a) A schematic for the cantilever unimorph subjected to uniformly distributed load (C-Q case), which is discussed in section 3.4. (b) FEM results of $\sigma_1$ and $P_3$ when $q_c = 15\ \mathrm{N\ m^{-1}}$. (c), (d) The analytical and FEM results of normalized voltage, charge density, and energy density as functions of the thickness ratio. Dash–dot curves do not account for $d_{33}$ effects, whereas solid curves do. (e), (f) The analytical and FEM results of normalized voltage, charge density, and energy density as functions of the thickness ratio when the piezo-layer and substrate are flipped. Dash–dot curves do not account for $d_{33}$ effects, whereas solid curves do.

figures 5(e) and (f). The optimal $\eta$ for maximum voltage and energy density outputs are 0.44 and 0.18, respectively.

### *3.5. Cantilever unimorph subjected to point load at the end (C–F)*

Point load is an easily achievable loading condition in experiment. As depicted in figure 6(a), a point load ($F_c$) is applied at the end of the cantilever unimorph. The moment distribution in the cantilever can be expressed by

$$M(x) = F_c(L - x). \tag{23}$$

After averaging equation (23) over $L$ and substituting the result $F_cL/2$ into $M_0$ in equation (7), the charge density and the voltage output without accounting for $\sigma_3$ contribution can be readily obtained as

$$\rho_{\mathrm{C-F}} = \frac{d_{31}F_cL}{2{h_2}^2}\left[\frac{\Sigma}{\bar{I}}\left(1+\frac{\eta}{2}-\Delta\eta\right)\right] \tag{24}$$

and

$$V_{\mathrm{C-F}} = \frac{d_{31}F_cL}{2\varepsilon_p{}'h_2}\left[\frac{\Sigma\eta}{\bar{I}}\left(1+\frac{\eta}{2}-\Delta\eta\right)\right]. \tag{25}$$

But as illustrated in figure 4(b), the C–F case has nonzero $\sigma_3$. Based on the equation given in figure 4(b), $\sigma_3$ and the

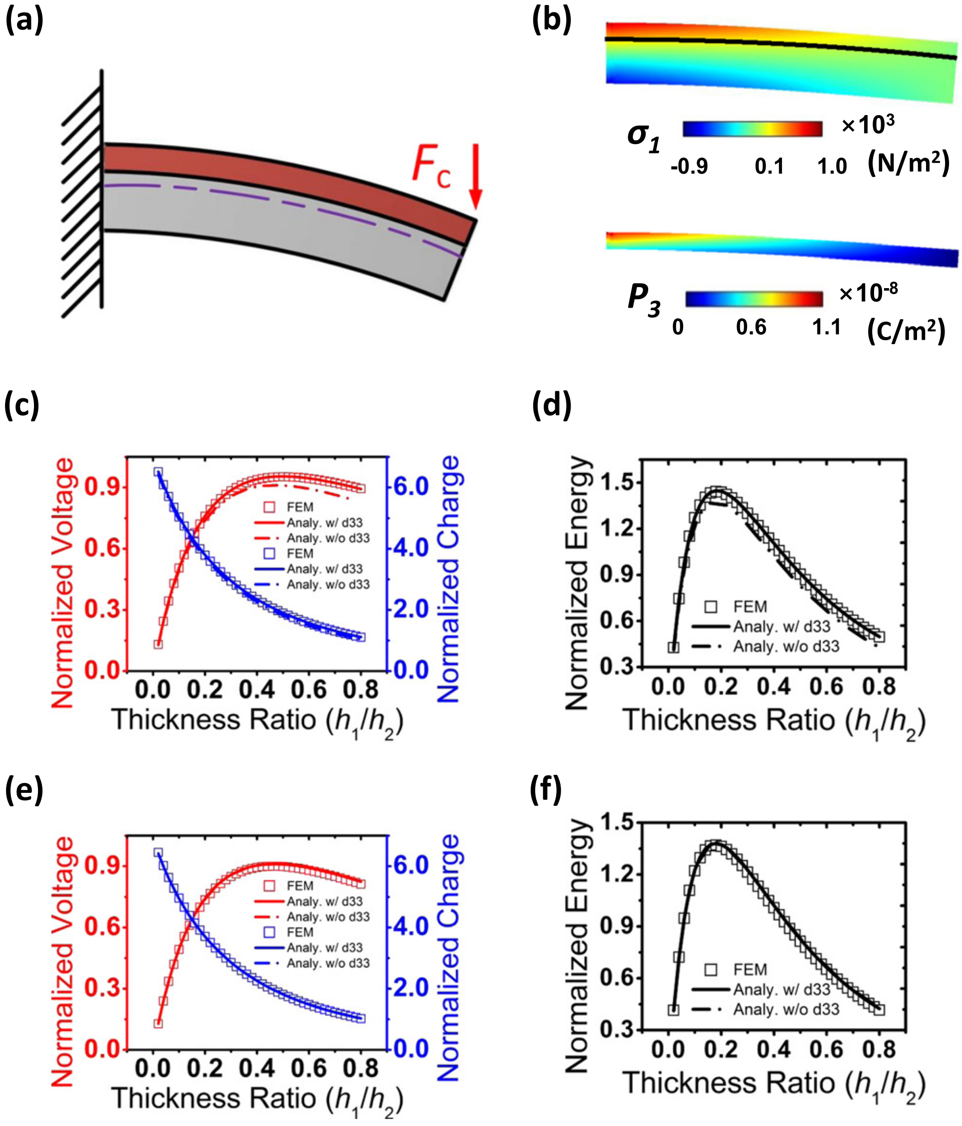

**Figure 6.** (a) A schematic for the cantilever unimorph subjected to point load (C–F case), which is discussed in section 3.5. (b) FEM results of $\sigma_1$ and $P_3$ when $F_c = 1$ mN. (c), (d) The analytical and FEM results of normalized voltage, charge density, and energy density as functions of the thickness ratio. Dash–dot curves do not account for $d_{33}$ effects, whereas solid curves do. (e), (f) The analytical and FEM results of normalized voltage, charge density, and energy density as functions of the thickness ratio when the piezo-layer and substrate positions are flipped. Dash–dot curves do not account for $d_{33}$ effects, whereas solid curves do.

resulted polarization in the C–F condition are given by

$$\sigma_3 = -\frac{F_c}{L}\left\{1 - \frac{1}{\bar{I}}\left[\frac{1}{3}(1+\eta-\Delta\eta)^3 - \frac{1}{2}(1+\eta-\Delta\eta)^2\left(\frac{z}{h_2}-\Delta\eta\right) + \frac{1}{6}\left(\frac{z}{h_2}-\Delta\eta\right)^3\right]\right\} \quad (26)$$

and

$$P_{3\_d_{33}} = -d_{33}\frac{F_c}{L}\left\{1 - \frac{1}{\bar{I}}\left[\frac{1}{3}(1+\eta-\Delta\eta)^3 - \frac{1}{2}(1+\eta-\Delta\eta)^2\left(\frac{z}{h_2}-\Delta\eta\right) + \frac{1}{6}\left(\frac{z}{h_2}-\Delta\eta\right)^3\right]\right\}, \quad (27)$$

respectively. The total charge density and voltage output induced by both $\sigma_1$ and $\sigma_3$ in the C–F case are therefore

$$\rho'_{\mathrm{C-F}} = \frac{d_{31}F_{\mathrm{c}}L}{2{h_2}^2}\left\{\frac{\Sigma}{\bar{I}}\left[\left(1+\frac{\eta}{2}-\Delta\eta\right)-\frac{d_{33}}{d_{31}}\left(\frac{h_2}{L}\right)^2 \times\left(\frac{12\bar{I}-\eta^2(3+2\eta-3\Delta\eta)}{6\Sigma}\right)\right]\right\} \tag{28}$$

and

$$V'_{\mathrm{C-F}} = \frac{d_{31}F_{\mathrm{c}}L}{2{\varepsilon_{\mathrm{p}}}'h_2}\left\{\frac{\Sigma\eta}{\bar{I}}\left[\left(1+\frac{\eta}{2}-\Delta\eta\right)-\frac{d_{33}}{d_{31}}\left(\frac{h_2}{L}\right)^2 \times\left(\frac{12\bar{I}-\eta^2(3+2\eta-3\Delta\eta)}{6\Sigma}\right)\right]\right\}. \tag{29}$$

Figure 6(b) shows the FEM results of $\sigma_1$ and $P_3$ when the piezo-film is 10 $\mu$m thick and the averaged moment equals to the $M_0$ used in the PB-M case. To reduce the singularity error of FEM, the point load is located $L/200$ away from the end edge of the cantilever because if the point load is applied exactly on the end edge of the unimorph, the COMSOL Multiphysics only applies half of the load to the unimorph. This technique of leaving a small margin towards the end is also applied to other FEM simulations which have loadings applied up to the edge, including distributed loads and applied displacement.

The comparison between FEM and analytical solution is made in figures 6(c) and (d). The good agreement also validates our rationale that there is $\sigma_3$ contribution in C–F case. Comparing figures 5(c) and (d) with 6(c) and (d), it is concluded that the $d_{33}$ effect on the electric outputs of C–Q is greater than that of C–F. This is because $\sigma_3$ of C–Q is three times greater than that of C–F as we dictated $F_{\mathrm{c}}L/2 = q_{\mathrm{c}}L^2/6 = M_0$. The optimal $\eta$ for the voltage and the energy density were 0.5 and 0.18, respectively.

Similar to figures 5, 6(e) and (f) show the normalized electrical outputs when film and substrate are flipped. The $\sigma_3$ contribution will again counteract the $\sigma_1$ contribution but the effect of $\sigma_3$ is much less significant than the C–Q case. The optimal $\eta$ for the voltage and the energy density are 0.46 and 0.18, respectively, which are the same as the PB-M case.

### *3.6. Cantilever unimorph subjected to fixed end displacement (C–W)*

Figure 7 offers the FEM and analytical results for the C–W unimorph as depicted in figure 7(a). Plugging the cantilever load–displacement relation: $F = 3\bar{Y}_2 I w_{\mathrm{c}}/(2L^3)$ into equation (23), the moment in the cantilever can be expressed as

$$M(x) = \frac{3\bar{Y}_2 I w_{\mathrm{c}}}{2L^3}(L-x). \tag{30}$$

Following the same procedure outlined before we can apply equation (30) to calculate the charge density and the voltage outputs just induced by $\sigma_1$ as

$$\rho_{\mathrm{C-W}} = d_{31}\bar{Y}_1\kappa_1 h_2\left(1+\frac{\eta}{2}-\Delta\eta\right) \tag{31}$$

and

$$V_{\mathrm{C-W}} = \frac{d_{31}\bar{Y}_1\kappa_1{h_2}^2}{\varepsilon'_{\mathrm{p}}}\left[\eta\left(1+\frac{\eta}{2}-\Delta\eta\right)\right], \tag{32}$$

respectively. Similar to the C–F case, the modified charge density and voltage of C–W condition with the $d_{33}$ effect included are given by

$$\rho'_{\mathrm{C-W}} = d_{31}\bar{Y}_1\kappa_1 h_2\left[\left(1+\frac{\eta}{2}-\Delta\eta\right)-\frac{d_{33}}{d_{31}}\left(\frac{h_2}{L}\right)^2 \times\left(\frac{12\bar{I}-\eta^2(3+2\eta-3\Delta\eta)}{6\Sigma}\right)\right] \tag{33}$$

and

$$V'_{\mathrm{C-W}} = \frac{d_{31}\bar{Y}_1\kappa_1{h_2}^2}{{\varepsilon_{\mathrm{p}}}'}\left\{\eta\left[\left(1+\frac{\eta}{2}-\Delta\eta\right) - \frac{d_{33}}{d_{31}}\left(\frac{h_2}{L}\right)^2\left(\frac{12\bar{I}-\eta^2(3+2\eta-3\Delta\eta)}{6\Sigma}\right)\right]\right\}, \tag{34}$$

respectively.

Figure 7(b) shows the FEM result of $\sigma_1$ and $P_3$ under the C–W condition when the piezo-layer is 10 $\mu$m thick, the unimorph is 200 $\mu$m long, and $w_{\mathrm{c}} = 53.3$ nm such that the average curvature, $\kappa_1 = 3w_{\mathrm{c}}/2L^2$, is the same as the $\kappa_0 = 2\ \mathrm{m}^{-1}$ used for the PB-$\kappa$ case.

The normalized voltage, charge and energy density of the piezo-layer-on-substrate case are plotted in figures 7(c) and (d) and that of the substrate-on-piezo-layer case are offered in figures 7(e) and (f). Although the $d_{33}$ effect is included as solid curves in both cases, the $\sigma_3$ contribution is small within the current range of $h_1/h_2$ and the results are very similar to the PB-$\kappa$ results. But when $h_1/h_2$ gets very large (e.g. larger than 4), the voltage and energy density curves in figures 7(e) and (f) will become non-monotonic.

It is interesting to notice that the C–F results (figure 6) are very similar to the PB-M results (figure 2) and the C–W results (figure 7) are very similar to the PB-$\kappa$ results (figure 3), we can conclude that the pure bending condition and cantilever subjected to end load condition are almost equivalent except that the $d_{33}$ effect in cantilever unimorphs has to be accounted for when $h_2/L$ is large. More discussions on $h_2/L$ effect will be given in sections 3.9 and 4.1.

### *3.7. Simply supported unimorph with uniformly distributed load (SS–Q)*

Simple support is another popular boundary condition for beams. When subjected to uniformly distributed load $q_{\mathrm{s}}$ as illustrated in figure 8(a), the moment function can be written as

$$M(x) = \frac{q_{\mathrm{s}}x}{2}(L-x). \tag{35}$$

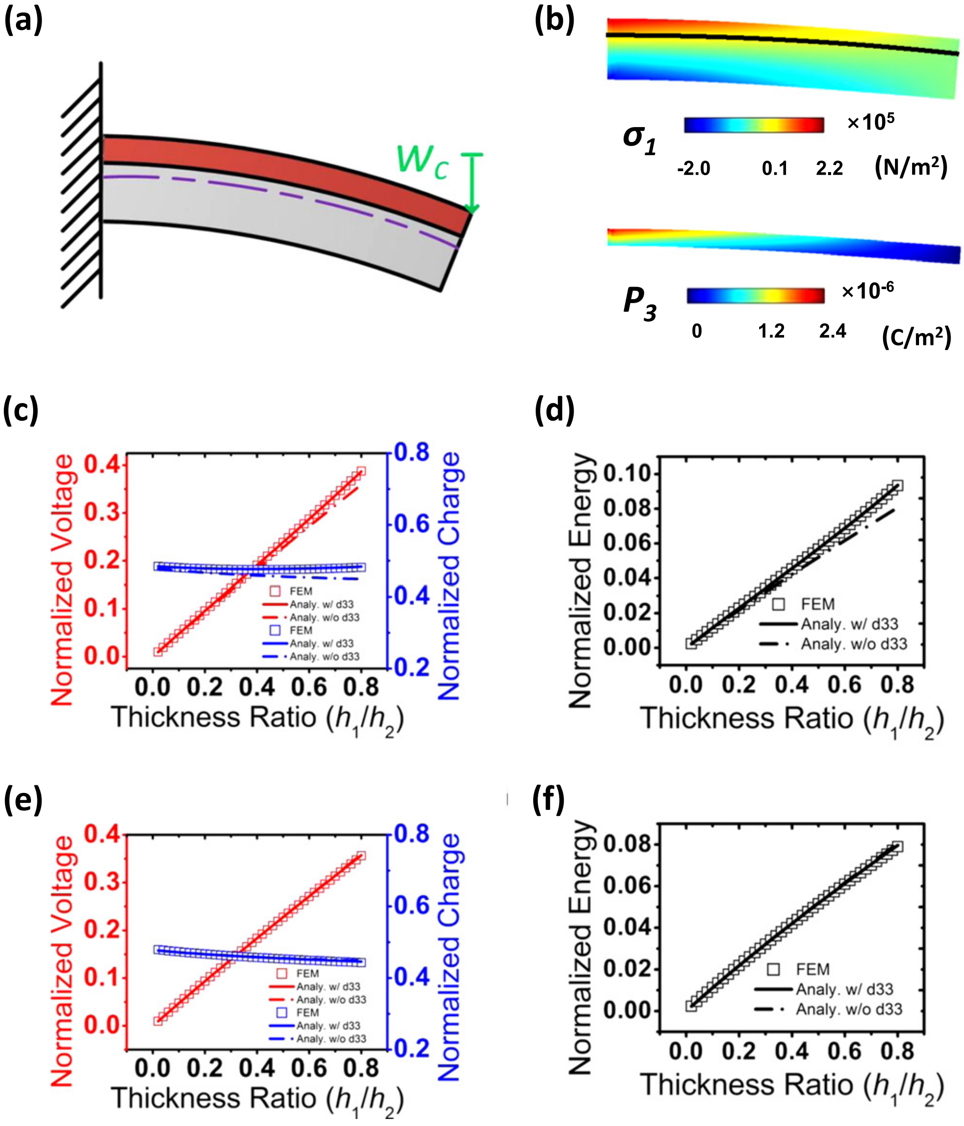

**Figure 7.** (a) A schematic for the cantilever unimorph subjected to end displacement (C–W case), which is discussed in section 3.6. (b) FEM results of $\sigma_1$ and $P_3$ when $w_c = 53.3$ nm. (c), (d) The analytical and FEM results of normalized voltage, charge density, and energy density as functions of the thickness ratio. Dash–dot curves do not account for $d_{33}$ effects, whereas solid curves do. (e), (f) The analytical and FEM results of normalized voltage, charge density, and energy density as functions of the thickness ratio when the piezo-layer and substrate positions are flipped. Dash–dot curves do not account for $d_{33}$ effects, whereas solid curves do.

Hence the charge density and the voltage output induced by $\sigma_1$ are obtained using equations (7) and (35) as

$$\rho_{\mathrm{SS-Q}} = \frac{d_{31} q_{\mathrm{s}} L^2}{12 {h_2}^2}\left[\frac{\Sigma}{\bar{I}}\left(1 + \frac{\eta}{2} - \Delta\eta\right)\right] \tag{36}$$

and

$$V_{\mathrm{SS-Q}} = \frac{d_{31} q_{\mathrm{s}} L^2}{12 \varepsilon_{\mathrm{p}}{}' h_2}\left[\frac{\Sigma\eta}{\bar{I}}\left(1 + \frac{\eta}{2} - \Delta\eta\right)\right], \tag{37}$$

respectively. Comparing equations (36) and (37) with (17) and (18), SS–Q is equivalent to C–Q if $q_{\mathrm{s}} = q_{\mathrm{c}}/2$. Therefore similar to the C–Q case, SS–Q should also account for the effect of $\sigma_3$ as calculated in figure 4(c) and the modified charge density and voltage become

$$\rho'_{\mathrm{SS-Q}} = \frac{d_{31} q_{\mathrm{c}} L^2}{12 {h_2}^2}\left\{\frac{\Sigma}{\bar{I}}\left[\left(1 + \frac{\eta}{2} - \Delta\eta\right) + \frac{d_{33}}{d_{31}}\left(\frac{h_2}{L}\right)^2\left(\frac{12\bar{I}}{\Sigma}\right)\right]\right\} \tag{38}$$

and

$$V'_{\mathrm{SS-Q}} = \frac{d_{31} q_{\mathrm{c}} L^2}{12 \varepsilon_{\mathrm{p}}{}' h_2}\left\{\frac{\Sigma\eta}{\bar{I}}\left[\left(1 + \frac{\eta}{2} - \Delta\eta\right) + \frac{d_{33}}{d_{31}}\left(\frac{h_2}{L}\right)^2\left(\frac{12\bar{I}}{\Sigma}\right)\right]\right\}. \tag{39}$$

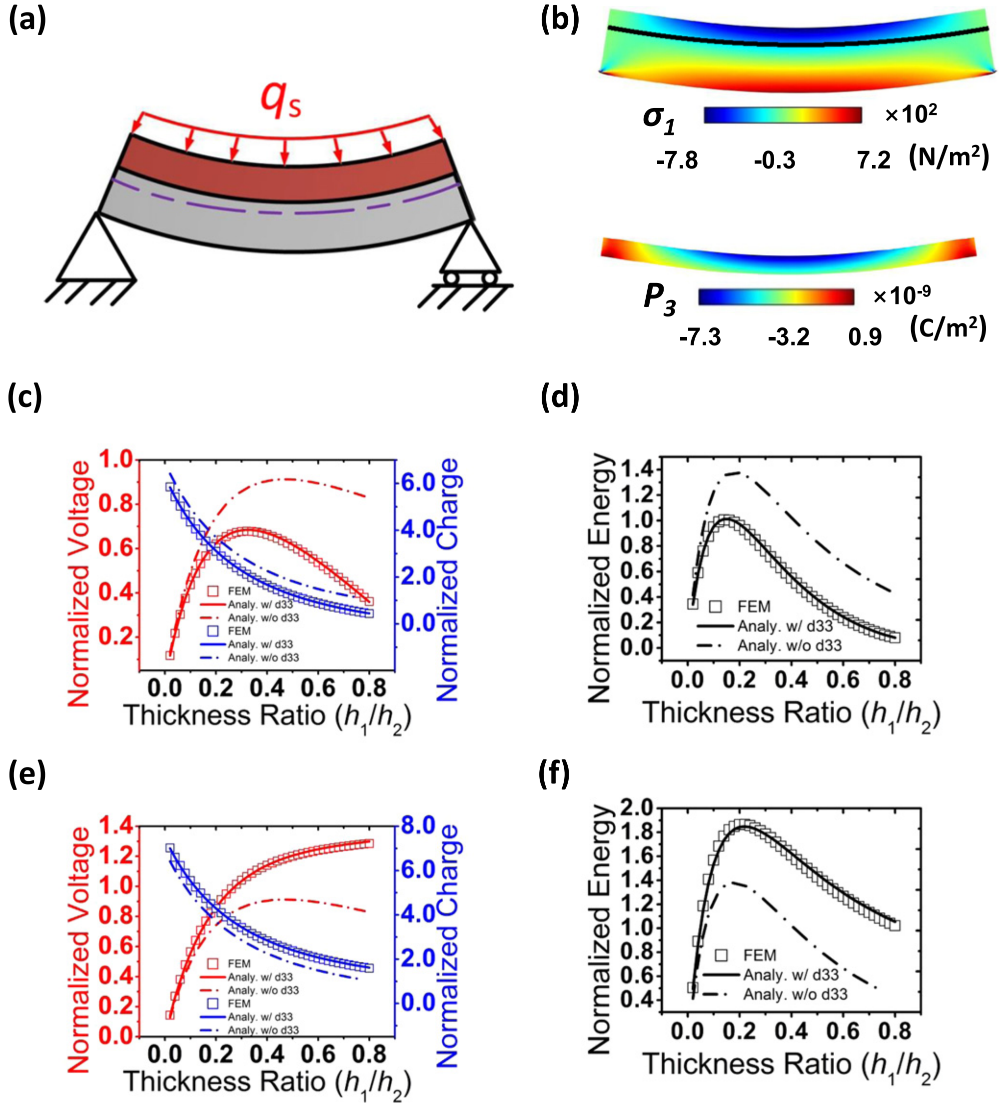

**Figure 8.** (a) A schematic for the simply supported unimorph subjected to uniformly distributed load (SS–Q case), which is discussed in section 3.7. (b) FEM results of $\sigma_1$ and $P_3$ when $q_s = 30\ \mathrm{N\ m^{-1}}$. (c), (d) The analytical and FEM results of normalized voltage, charge density, and energy density as functions of the thickness ratio. Dash–dot curves do not account for $d_{33}$ effects, whereas solid curves do. (e), (f) The analytical and FEM results of normalized voltage, charge density, and energy density as functions of the thickness ratio when the piezo-layer and substrate positions are flipped. Dash–dot curves do not account for $d_{33}$ effects, whereas solid curves do.

In equations (38) and (39), the $d_{33}$ term always vanishes as $h_2/L$ decreases, which is similar to the C–Q case. However, unlike the C–Q case, the $d_{33}$ term minifies both charge density and voltage output since $\sigma_1$ in the piezo-layer is negative in the SS–Q case. This effect is clearly observable in figures 8(c) and (d), where the solid curves that account for the $d_{33}$ effects are much lower than the dash–dot curves and demonstrate much better agreement with the FEM results. In this case, the optimal $\eta$ for the voltage and the energy outputs are 0.32 and 0.14, respectively.

Similar to the C–Q case that the $d_{33}$ effect presents in this boundary/loading condition, we also provide the solutions when the piezo-layer and the substrate are flipped, as shown in figures 8(e) and (f). Now the $d_{33}$ effect enhances the output as expected and its contribution is as significant as the piezo-layer-on-substrate case. For the given range of $h_1/h_2$, the voltage curve is monotonic and hence there is no optimal $\eta$ for the voltage output. If the beam length increases, there would be an optimal $\eta$ which will be similar to the C–Q case. The optimal $\eta$ for the energy density is 0.22.

### *3.8. Simply supported unimorph subjected to point load at the center (SS–F)*

Figure 9 shows the results for the SS–F case. As the point load $F_s$ is applied at the middle of the beam, the analytical expression of the moment is given by

$$M(x) = \begin{cases} \dfrac{F_s x}{2} & \text{for } 0 \leqslant x \leqslant \dfrac{L}{2} \\ \dfrac{F_s (L - x)}{2} & \text{for } \dfrac{L}{2} \leqslant x \leqslant L \end{cases}. \tag{40}$$

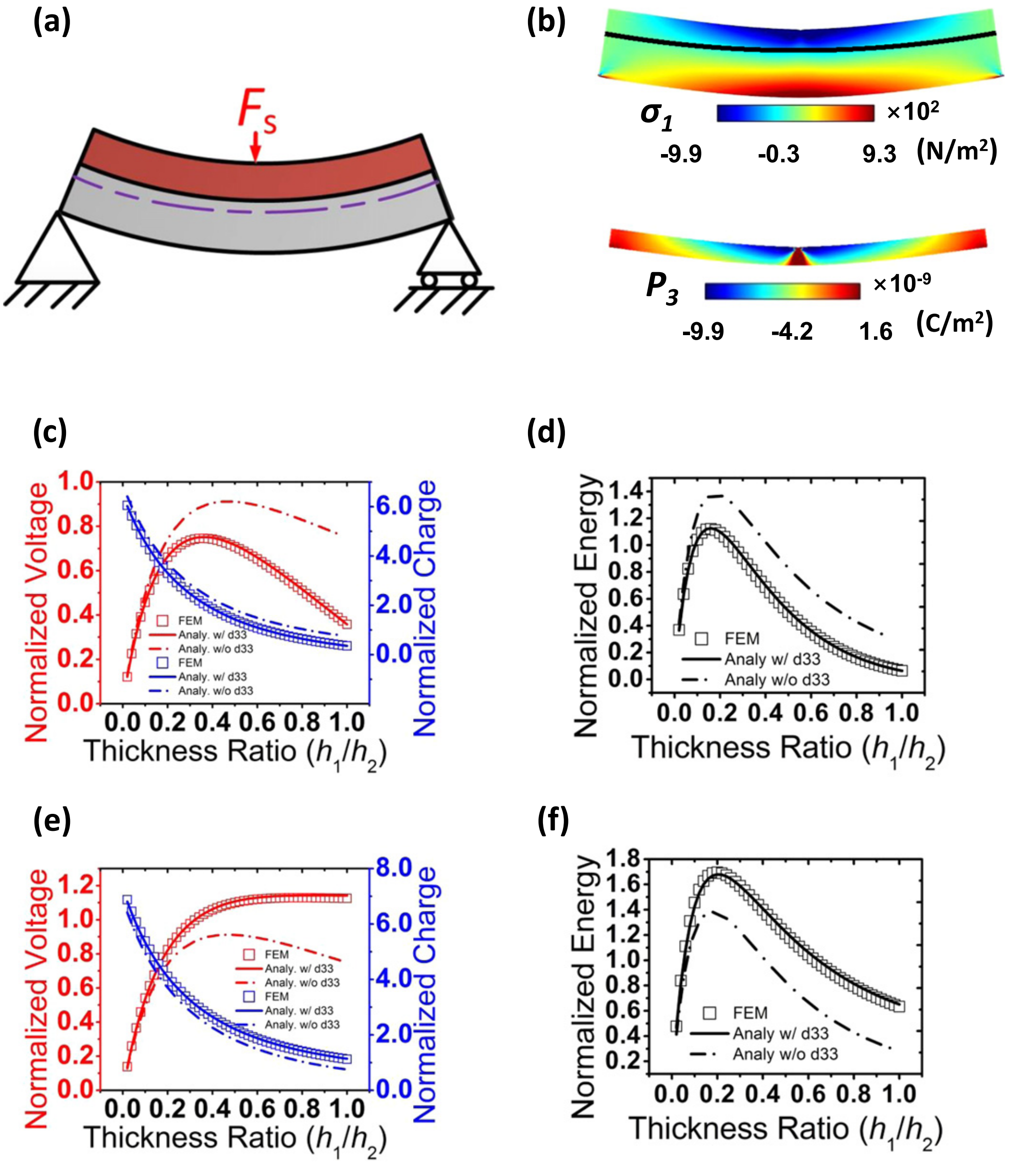

**Figure 9.** (a) A schematic for the simply supported unimorph subjected to point load (SS–F case), which is discussed in section 3.8. (b) FEM results of $\sigma_1$ and $P_3$ when $F_{\mathrm{s}} = 4$ mN. (c), (d) The analytical and FEM results of normalized voltage, charge density, and energy density as functions of the thickness ratio. Dash–dot curves do not account for $d_{33}$ effects, whereas solid curves do. (e), (f) The analytical and FEM results of normalized voltage, charge density, and energy density as functions of the thickness ratio when the piezo-layer and substrate positions are flipped. Dash–dot curves do not account for $d_{33}$ effects, whereas solid curves do.

Following the same procedure introduced in section 3.5, the charge density and voltage outputs just induced by $\sigma_1$ are

$$\rho_{\mathrm{SS-F}} = \frac{d_{31}F_{\mathrm{s}}L}{8{h_2}^2}\left[\frac{\Sigma}{\bar{I}}\left(1+\frac{\eta}{2}-\Delta\eta\right)\right] \tag{41}$$

and

$$V_{\mathrm{SS-F}} = \frac{d_{31}F_{\mathrm{s}}L}{8\varepsilon_{\mathrm{p}}{}'h_2}\left[\frac{\Sigma\eta}{\bar{I}}\left(1+\frac{\eta}{2}-\Delta\eta\right)\right]. \tag{42}$$

The effective moment term in the SS–F case is $F_{\mathrm{s}}L/8$ while that of the C–F case is $F_{\mathrm{c}}L/2$. If the effective moments are required to be equal, then $F_{\mathrm{s}} = 4F_{\mathrm{c}}$. Figure 9(b) shows the FEM results of $\sigma_1$ and $P_3$, when the piezo-layer is 10 $\mu$m thick and $F_{\mathrm{s}} = 4F_{\mathrm{c}}$, where $F_{\mathrm{c}}$ is the end point load applied in the C–F case. The magnitude of $\sigma_1$ is similar to that in the C–F case, except the sign is opposite. To account for the effect of $\sigma_3$ as illustrated in figure 4(d), we need to modify equations (41) and (42) to be

$$\rho'_{\mathrm{SS-F}} = \frac{d_{31}q_{\mathrm{c}}L^2}{8{h_2}^2}\left\{\frac{\Sigma}{\bar{I}}\left[\left(1+\frac{\eta}{2}-\Delta\eta\right) + \frac{d_{33}}{d_{31}}\left(\frac{h_2}{L}\right)^2\left(\frac{8\bar{I}}{\Sigma}\right)\right]\right\} \tag{43}$$

and

$$V'_{\mathrm{SS-F}} = \frac{d_{31} q_c L^2}{8 {\varepsilon_\mathrm{p}}' h_2}\left\{\frac{\Sigma\eta}{\bar{I}}\left[\left(1+\frac{\eta}{2}-\Delta\eta\right) + \frac{d_{33}}{d_{31}}\left(\frac{h_2}{L}\right)^2\left(\frac{8\bar{I}}{\Sigma}\right)\right]\right\}. \tag{44}$$

In equations (43) and (44), the $d_{33}$ term always vanishes as $h_2/L$ decreases, which is similar to the SS–Q case. However, the polarization density induced by $\sigma_3$ in the SS–F case is less than that of SS–Q. To achieve the same effective moment, we need $q_\mathrm{s} = 3F_\mathrm{s}/(2L)$, which means SS–Q case has 1.5 times larger effective $\sigma_3$ than the SS–F case. The same conclusion can also be made by comparing the coefficient of the $d_{33}$ term between equations (38) and (43): 12 in SS–Q case versus 8 in the SS–F case. Therefore, the electric output variation caused by the $d_{33}$ effect in SS–Q is greater than that in SS–F, which can be observed from the comparison between figures 8(c) and 9(c). The optimal $\eta$ for maximum voltage and the energy density outputs are 0.36 and 0.16, respectively in figures 9(c) and (d). When piezo layer and substrate are flipped, figures 9(e) and (f) suggest the optimal $\eta$ are 0.84 for maximum voltage output and 0.2 for maximum energy density output, respectively.

### *3.9. Simply supported unimorph subjected to fixed center displacement (SS–W)*

Figure 10(a) illustrates the SS–W condition where a simply supported unimorph is subjected to a fixed center displacement, $w_\mathrm{s}$. The load–displacement relation of a simply supported beam subjected to center load or displacement is $F = 48\bar{Y}_2 I w_\mathrm{s}/L^3$, therefore the moment function of the SS–W case can be obtained by substituting this new $F$ in equation (40):

$$M(x) = \begin{cases} \dfrac{24\bar{Y}_2 I w_\mathrm{s}}{L^3} x & \text{for } 0 \leqslant x \leqslant \dfrac{L}{2} \\ \dfrac{24\bar{Y}_2 I w_\mathrm{s}}{L^3}(L-x) & \text{for } \dfrac{L}{2} \leqslant x \leqslant L \end{cases}. \tag{45}$$

Following the same procedure in section 3.8 (the SS–F case), the analytical solutions for the charge density and the voltage output for the SS–W case without considering the $d_{33}$ effect are

$$\rho_{\mathrm{SS-W}} = d_{31}\bar{Y}_1 \kappa_2 h_2\left(1+\frac{\eta}{2}-\Delta\eta\right) \tag{46}$$

and

$$V_{\mathrm{SS-W}} = \frac{d_{31}\bar{Y}_1 \kappa_2 {h_2}^2}{{\varepsilon_\mathrm{p}}'}\left[\eta\left(1+\frac{\eta}{2}-\Delta\eta\right)\right], \tag{47}$$

respectively. When the $d_{33}$ effect is considered as in the SS–F case, equations (46) and (47) have to be modified to

$$\rho'_{\mathrm{SS-W}} = d_{31}\bar{Y}_1 \kappa_2 h_2\left[\left(1+\frac{\eta}{2}-\Delta\eta\right) + \frac{d_{33}}{d_{31}}\left(\frac{h_2}{L}\right)^2\left(\frac{8\bar{I}}{\Sigma}\right)\right] \tag{48}$$

and

$$V'_{\mathrm{SS-W}} = \frac{d_{31}\bar{Y}_1 \kappa_2 {h_2}^2}{{\varepsilon_\mathrm{p}}'}\left\{\eta\left[\left(1+\frac{\eta}{2}-\Delta\eta\right) + \frac{d_{33}}{d_{31}}\left(\frac{h_2}{L}\right)^2\left(\frac{8\bar{I}}{\Sigma}\right)\right]\right\}, \tag{49}$$

respectively. Figure 10(b) shows the FEM results of $\sigma_1$ and $P_3$ distribution under the SS–W condition when $w_\mathrm{s} = 13.3$ nm, which is chosen to ensure that the average curvature $\kappa_2 = 6w_\mathrm{s}/L^2$ is the same as the $\kappa_0 = 2\,\mathrm{m}^{-1}$ used for the PB-$\kappa$ case. Without considering the $d_{33}$ effect, the normalized electric outputs are plotted as dash–dot curves in figures 10(c) and (d), which are similar to the solid curves in the PB-$\kappa$ cases but very different from the FEM results. When the $d_{33}$ effect is considered, the solid curves find much better agreement with the FEM outputs. When piezo-layer is on top of the substrate, the $d_{33}$ effect minifies the outputs as $d_{33}$ is negative. Consequently, the optimal $\eta$ for maximum voltage output is 0.84 and 0.62 for maximum energy density. Since both voltage and charge density drop below 0 as $\eta$ increases, we extend the range of $\eta$ to 2 and find that as $\eta$ increases, the energy density drops to a minimum after reaching a maximum, and then takes off again. This behavior is distinctly different from PB-$\kappa$ case where voltage, charge density, and energy density are always monotonically increasing with $\eta$. Still, as $L$ increases, the $d_{33}$ effect will diminish according to equations (48) and (49).

Because there is the $d_{33}$ effect in the SS–W case, swapping piezo-layer and substrate would yield different outputs, as shown in figures 10(e) and (f). All three outputs are monotonic in this case because the $\sigma_1$ and $\sigma_3$ contributions have the same sign. The $d_{33}$ effect is clearly visible in this case, but now enhances the outputs.

## 4. Discussions

### *4.1. Effects of $Y_1/Y_2$ and $h_2/L$*

Throughout section 3, the elastic mismatch, $\Sigma = \bar{Y}_1/\bar{Y}_2$, has been fixed to be 1.148 for unimorphs composed of PVDF-TrFE bonded to Kapton. Here we would like to investigate the effects of $\Sigma$. As Wang *et al* [22] described, the optimal thickness ratio $\eta$ of unimorph cantilevers also varies with $\Sigma$.

Figure 11 plots the normalized voltage, charge density, and energy density as functions of $\eta$ in log–log scale under various $\Sigma$ for the PB-M condition in which case $d_{33}$ plays no role. As can be seen in figure 11(a) (plotted from equation (11)), (b) (plotted from equation (9)) and (c) (plotted

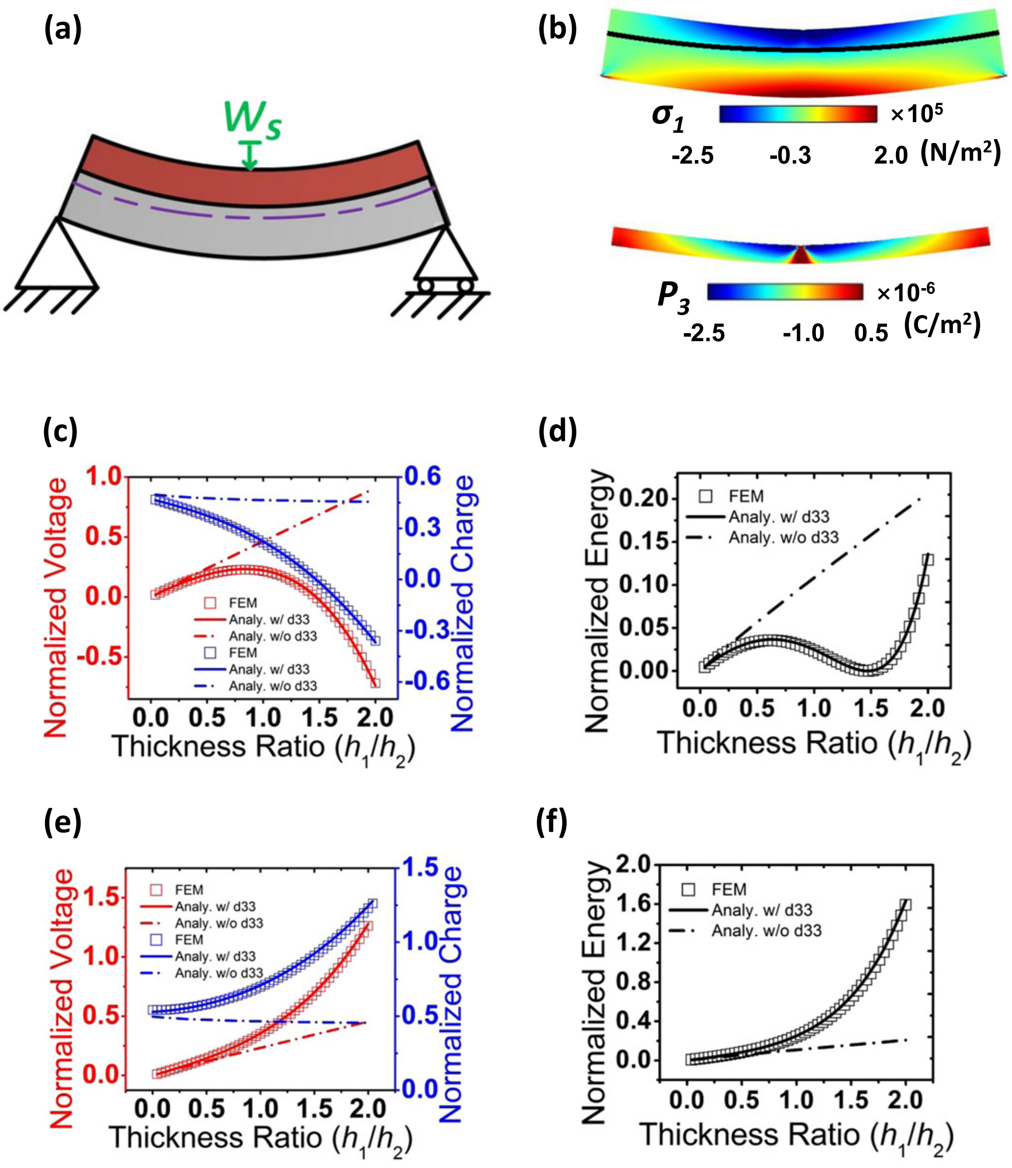

**Figure 10.** (a) A schematic for the simply supported unimorph subjected to central displacement (SS–W case), which is discussed in section 3.9. (b) FEM results of $\sigma_1$ and $P_3$ when $w_s = 13.3$ nm. (c), (d) The analytical and FEM results of normalized voltage, charge density, and energy density as functions of the thickness ratio. Dash–dot curves do not account for $d_{33}$ effects, whereas solid curves do. (e), (f) The analytical and FEM results of normalized voltage, charge density, and energy density as functions of the thickness ratio when the piezo-layer and substrate positions are flipped. Dash–dot curves do not account for $d_{33}$ effects, whereas solid curves do.

from equation (12)), the optimal $\eta$ shifts to the left as $\Sigma$ increases in all electric output cases and are in general different for different outputs. When $\eta$ is small (i.e. $\eta \ll 1$), the larger $\Sigma$ always yields the higher output but when $\eta$ is large, larger outputs are achieved for smaller $\Sigma$.

The effect of $h_2/L$ is also investigated because it is a component that always appears in the $d_{33}$ term. When $h_2/L \ll 1$, the $d_{33}$ effect is negligible but when $h_2/L$ is finite, the $d_{33}$ effect sometimes can become obvious or even overwhelms $\sigma_1$ contribution. Figures 11(d), (e), and (f) plot normalized voltage, charge density, and energy density as functions of $\eta$ under various $h_2/L$ for the SS–Q condition. For voltage and energy density, the optimal $\eta$ shifts slightly to the right as $h_2/L$ decreases and stabilizes when $h_2/L$ drops below $1/20$, which is consistent with the observation in [39]. Similar plots can be constructed for other boundary/loading conditions which have to account for the $d_{33}$ effect.

### *4.2. Unimorph actuators*

Thickness ratio variation also affects the displacement of a unimorph subjected to applied electric field [40] as shown in figure 12. By applying the electric field $E = V_0/h_1$ across the thickness direction of the piezoelectric layer, a uniform longitudinal strain is induced in the piezoelectric layer. Consequently the magnitude of the longitudinal stress within the piezoelectric layer is $\sigma_1 = d_{31}\overline{Y_1}V_0/h_1$,

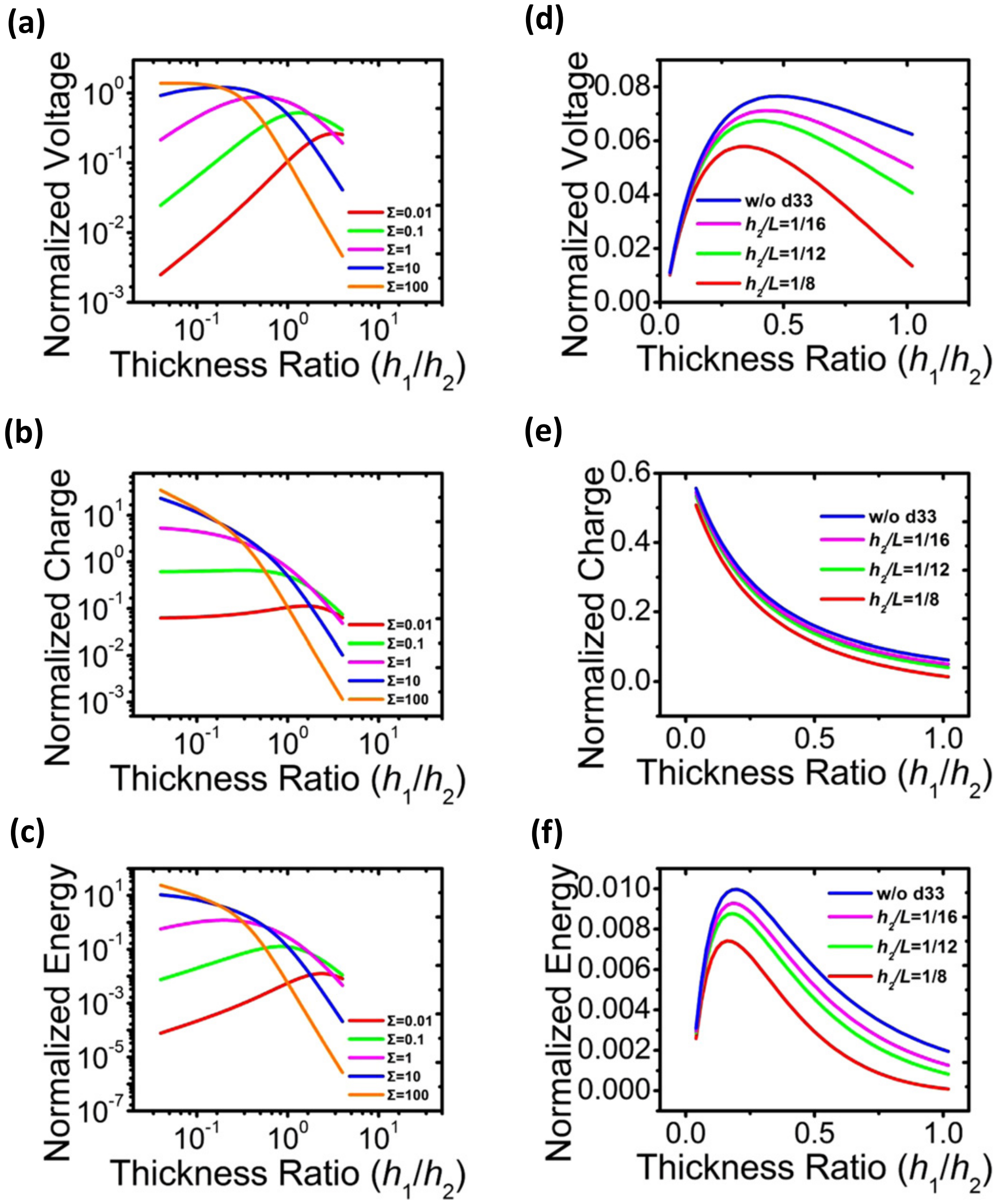

**Figure 11.** (a)–(c) The effects of stiffness ratio on the normalized voltage, charge density, and energy density under the PB-M condition. (d)–(f) The effects of substrate thickness-to-length ratio on the normalized voltage, charge density, and energy density under the SS–Q condition.

while the stress at the substrate layer remains zero. Therefore, the resultant moment of the unimorph can be written as

$$M_{\mathrm{E}} = \int_{h_2}^{h_1+h_2} d_{31}\bar{Y}_1 V_0 \cdot \left(\frac{z}{h_1} - \Delta\right)\mathrm{d}z, \tag{50}$$

which is calculated to be

$$M_{\mathrm{E}} = d_{31}\bar{Y}_1 V_0 h_2\left[\left(1 + \frac{\eta}{2} - \Delta\eta\right)\right]. \tag{51}$$

Hence, the maximum displacement of the simply supported unimorph subjected to constant voltage (SS–V) as shown in figure 12(a) is

$$w_{\mathrm{s\_max}} = \frac{d_{31}V_0L^2}{8{h_2}^2}\left\{\frac{\Sigma}{\bar{I}}\left[\left(1 + \frac{\eta}{2} - \Delta\eta\right) + \frac{d_{33}}{d_{31}}\left(\frac{h_2}{L}\right)^2\left(\frac{8\bar{I}}{\Sigma}\right)\right]\right\}. \tag{52}$$

The second term in equation (52) accounts for the thickness direction deformation from $\sigma_3$ induced by the constant electric potential.

Figure 12(b) plots the normalized maximum actuation displacement obtained from FEM and equation (52) with respect to the thickness ratio when $\Sigma$ is fixed to be 1.148. The $d_{33}$ effect slightly diminishes the displacement. The optimal thickness ratio for maximum displacement is 1.89.

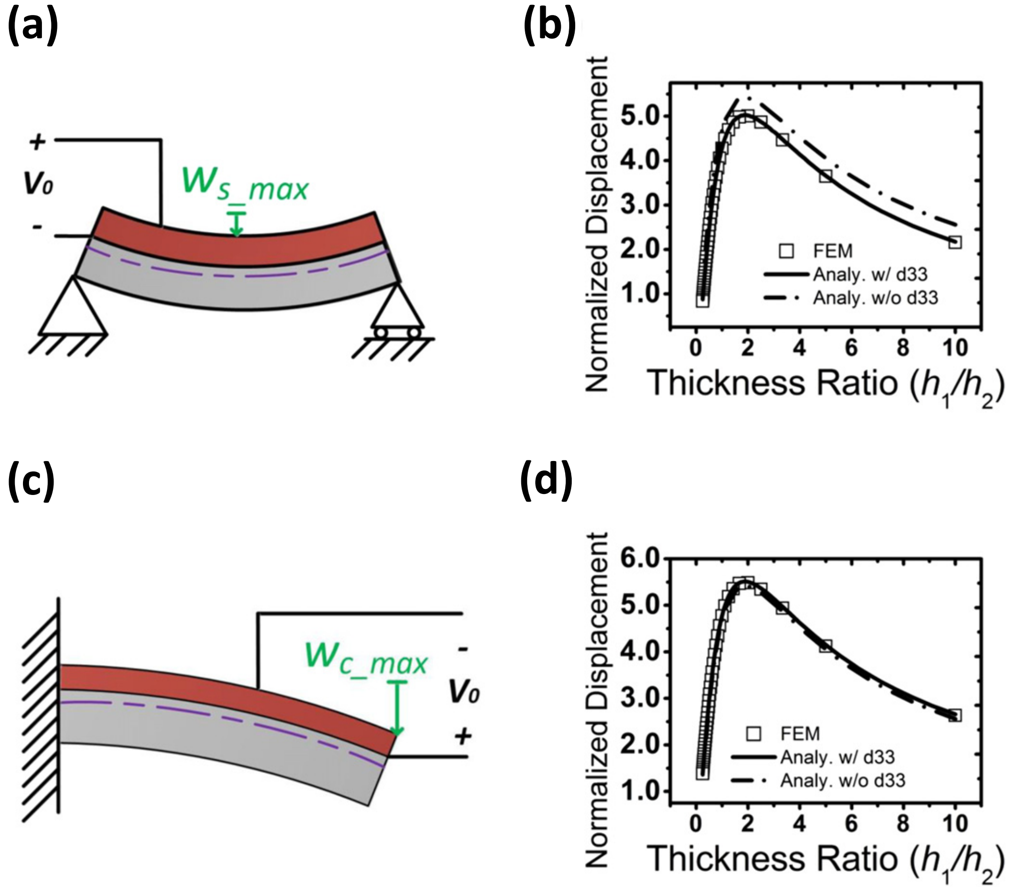

**Figure 12.** (a) A schematic of a simply supported unimorph actuator subjected to constant electric potential (SS–V case). (b) The analytical and FEM results of normalized maximum displacement of the unimorph as a function of the thickness ratio. Dash–dot curves do not account for $d_{33}$ effects, whereas solid curves do. (c) A schematic of a cantilever unimorph actuator subjected to constant electric potential (C–V case). (d) The analytical and FEM results of normalized maximum displacement of the unimorph as a function of the thickness ratio. Dash–dot curves do not account for $d_{33}$ effects, whereas solid curves do.

Similarly, the maximum displacement of the cantilever unimorph subjected to constant electric potential (C–V) as shown in figure 12(c) is

$$w_{c\_\max} = \frac{d_{31}V_0L^2}{2{h_2}^2}\left\{\frac{\Sigma}{\bar{I}}\left[\left(1+\frac{\eta}{2}-\Delta\eta\right) - \frac{d_{33}}{d_{31}}\left(\frac{h_2}{L}\right)^2\left(\frac{2\bar{I}}{\Sigma}\right)\right]\right\}. \tag{53}$$

Figure 12(d) plots the normalized maximum displacement with respect to the thickness ratio. The optimal thickness ratio of the maximum displacement of the C–V is 1.89, which is the same as the SS–V case. The $\sigma_3$ effect is also considered in this case and it enlarges the displacement but is less significant compared to the SS–V case. Due to symmetry, the actuation of unimorphs under pure bending is identical to the C–V case.

It is worth mentioning that the moment induced by the applied electric potential does not equal any moment induced by the mechanical loadings as discussed in section 3 since the stress distributions are very different. Therefore, the generation mode and actuation mode of the same unimorph are not reciprocal to each other.

## 5. Conclusion

We investigate the electromechanical behaviors of flexible unimorph power generators and actuators. Analytical and numerical models are built to unveil the effects of piezo-layer-to-substrate thickness ratio and piezoelectric material constants on energy conversion under eight different boundary/loading conditions. Our theory reveals that when the unimorph is subjected to displacement-controlled loading conditions, the charge, voltage, and energy outputs are monotonic functions of the thickness ratio, whereas when the unimorph is subjected to load-controlled conditions, optimal thickness ratios for maximum voltage and energy outputs exist. Our linear piezoelectric theory has been fully validated by FEM. We have also found that except pure bending conditions, all cantilever and simply supported unimorphs should care about the $d_{33}$ (i.e. $\sigma_3$) contribution when the unimorph length is not much larger than the thickness. A simplified average stress model is proven effective in accounting for the $d_{33}$ effect. $d_{33}$ effect may also change the outputs of displacement controlled problems from monotonic to non-monotonic. The effects of elastic mismatch and thickness-to-length ratio have been discussed and analytical solutions for unimorph based actuators are also offered. This work provides a comprehensive and accurate solution for the design and optimization of unimorph based power generators and actuators.

## Acknowledgments

This work is supported by the NSF CMMI award under Grant No. 1351875 and the AFOSR award under Grant No. FA9550-15-1-0112 (PI: Lu). Partial financial support is also provided by National Science Foundation grants ECCS 1509369, ECCS 1309686 (PI: Zhang). TH is thankful to the Charles M Simmons Endowed Presidential Fellowship in Engineering from the University of Texas at Austin.

## References

[1] Tichy J 2010 *Fundamentals of Piezoelectric Sensorics: Mechanical, Dielectric, and Thermodynamical Properties of Piezoelectric Materials* (New York: Springer)
[2] Jaffe B, Cook W and Jaffe H 1971 *Piezoelectric Ceramics* (New York: Academic)
[3] Wang Z L and Song J H 2006 Piezoelectric nanogenerators based on zinc oxide nanowire arrays *Science* **312** 242–6
[4] Ma W H and Cross L E 2006 Flexoelectricity of barium titanate *Appl. Phys. Lett.* **88** 232902
[5] Kawai H 1969 Piezoelectricity of poly (vinylidene fluoride) *Japan. J. Appl. Phys.* **8** 975
[6] Paajanen M, Lekkala J and Kirjavainen K 2000 Electromechanical film (EMFi)—a new multipurpose electret material *Sensor Actuators* A **84** 95–102
[7] Ramadan K S, Sameoto D and Evoy S 2014 A review of piezoelectric polymers as functional materials for electromechanical transducers *Smart Mater. Struct.* **23** 033001
[8] Vijaya M S 2012 *Piezoelectric Materials and Devices: Applications in Engineering and Medical Sciences* (Boca Raton, FL: CRC Press)
[9] Li D J, Hong S, Gu S Y, Choi Y, Nakhmanson S, Heinonen O, Karpeev D and No K 2014 Polymer piezoelectric energy harvesters for low wind speed *Appl. Phys. Lett.* **104** 012902
[10] Molino-Minero-Re E, Carbonell-Ventura M, Fisac-Fuentes C, Manuel-Lazaro A and Toma D M 2012 Piezoelectric energy harvesting from induced vortex in water flow *2012 IEEE Int. Instrumentation and Measurement Technology Conf. (I2MTC)* pp 624–7
[11] Ishida K *et al* 2013 Insole pedometer with piezoelectric energy harvester and 2 V organic circuits *IEEE J. Solid-State Circuits* **48** 255–64
[12] Kim D H, Ghaffari R, Lu N S and Rogers J A 2012 Flexible and stretchable electronics for bio-integrated devices *Annu. Rev. Biomed. Eng.* **14** 113–28
[13] Qi Y and McAlpine M C 2010 Nanotechnology-enabled flexible and biocompatible energy harvesting *Energy Environ. Sci.* **3** 1275–85
[14] Qin Y, Wang X D and Wang Z L 2008 Microfibre-nanowire hybrid structure for energy scavenging *Nature* **451** 809–U5
[15] Qi Y, Nguyen T D, Purohit P K and McAlpine M C 2012 *Stretchable Electronics* (New York: Wiley) pp 111–39
[16] Park K I, Xu S, Liu Y, Hwang G T, Kang S J L, Wang Z L and Lee K J 2010 Piezoelectric BaTiO$_3$ thin film nanogenerator on plastic substrates *Nano Lett.* **10** 4939–43
[17] Dagdeviren C *et al* 2014 Conformal piezoelectric energy harvesting and storage from motions of the heart, lung, and diaphragm *Proc. Natl. Acad. Sci. USA* **111** 1927–32
[18] Hausler E, Stein L and Harbauer G 1984 Implantable physiological power supply with Pvdf film *Ferroelectrics* **60** 277–82
[19] Chen D J, Sharma T and Zhang J X J 2014 Mesoporous surface control of PVDF thin films for enhanced piezoelectric energy generation *Sensor Actuators* A **216** 196–201
[20] Chen D J and Zhang J X J 2015 Microporous polyvinylidene fluoride film with dense surface enables efficient piezoelectric conversion *Appl. Phys. Lett.* **106** 193901
[21] Chen D J, Wang C, Chen W, Chen Y Q and Zhang J X J 2015 PVDF-Nafion nanomembranes coated microneedles for in vivo transcutaneous implantable glucose sensing *Biosens. Bioelectron.* **74** 1047–52
[22] Wang Q M, Du X H, Xu B M and Cross L E 1999 Theoretical analysis of the sensor effect of cantilever piezoelectric benders *J. Appl. Phys.* **85** 1702–12
[23] Smits J G and Choi W S 1991 The constituent equations of piezoelectric heterogeneous bimorphs *IEEE Trans. Ultrason. Ferroelectr. Freq. Control* **38** 256–70
[24] Umeda M, Nakamura K and Ueha S 1996 Analysis of the transformation of mechanical impact energy to electric energy using piezoelectric vibrator *Japan. J. Appl. Phys.* **35** 3267–73
[25] Ng T H and Liao W H 2005 Sensitivity analysis and energy harvesting for a self-powered piezoelectric sensor *J. Intel. Mater. Syst. Struct.* **16** 785–97
[26] Li H D, Tian C and Deng Z D 2014 Energy harvesting from low frequency applications using piezoelectric materials *Appl. Phys. Rev.* **1** 041301
[27] Qiu Y *et al* 2015 Branched ZnO nanotrees on flexible fiber-paper substrates for self-powered energy-harvesting systems *Rsc Adv.* **5** 5941–5
[28] Guizzetti V F M, Marioli D and Zawada T 2009 Thickness optimization of a piezoelectric converter for energy harvesting *COMSOL Conf. (Milan)*
[29] Nechibvute A and Mudzingwa C 2013 The effect of substrate to piezoelectric thickness ratio on performance of unimorph sensor *Int. J. Eng. Res. Technol.* **2** 2678–82
[30] Jagtap S N and Paily R 2011 Geometry optimization of a MEMS-based energy harvesting device *Proc. 2011 IEEE Students' Technology Symp. (IIT Kharagpur)* pp 265–9
[31] Park J K and Moon W K 2005 Constitutive relations for piezoelectric benders under various boundary conditions *Sensor Actuators* A **117** 159–67
[32] Hutchinson J W and Suo Z 1992 Mixed-mode cracking in layered materials *Adv. Appl. Mech.* **29** 63–191
[33] Chen Q, Natale D, Neese B, Ren K L, Lin M R, Zhang Q M, Pattom M, Wang K W, Fang H F and Im E 2007 Piezoelectric polymers actuators for precise shape control of large scale space antennas—art. no. 65241P *Electroactive Polymer Actuators and Devices (EAPAD) 2007* vol 6524 pp P5241–5241
[34] Navid A, Lynch C S and Pilon L 2010 Purified and porous poly(vinylidene fluoride-trifluoroethylene) thin films for pyroelectric infrared sensing and energy harvesting *Smart Mater. Struct.* **19** 055006
[35] Wang H, Zhang Q M, Cross L E and Sykes A O 1993 piezoelectric, dielectric, and elastic properties of poly (vinylidene fluoride trifluoroethylene) *J. Appl. Phys.* **74** 3394–8

[36] Rogacheva N N 1994 *The Theory of Piezoelectric Shells and Plates* (Boca Raton, FL: CRC Press)

[37] Cowan N R 1964 The heart-lung coefficient and the transverse diameter of the heart *Br. Heart J.* **26** 116

[38] Dieudonn J M and Jean C F 1969 Epicardial strains during left ventricular contraction cycle *Am. J. Physiol.* **216** 1188

[39] Wang G 2013 Analysis of bimorph piezoelectric beam energy harvesters using Timoshenko and Euler–Bernoulli beam theory *J. Intel. Mater. Syst. Struct.* **24** 226–39

[40] Li X P, Shih W Y, Aksay I A and Shih W H 1999 Electromechanical behavior of PZT-brass unimorphs *J. Am. Ceram. Soc.* **82** 1733–40